

Scaling Relations of Strike-Slip Earthquakes with Different Slip-Rate-Dependent Properties at Depth

by G. Hillers and S. G. Wesnousky

Abstract Empirical observations suggest that earthquake stress drop is generally constant. To investigate the effect of rupture width on earthquake scaling relations, we analyze synthetic seismicity produced by a 3D vertical strike-slip fault model using two different profiles of frictional slip-rate behavior below the seismogenic zone. Within the rate-and-state framework, a relatively abrupt transition of the a - b profile from velocity weakening to strengthening at the base of the seismogenic crust produces increasing slip and stress drop with increasing event size. Choosing a smoother transition allows large earthquakes to propagate deeper, leading to similar slip-length scaling but constant stress-drop scaling. Our numerical experiments support the idea that the maintenance of constant stress drop across the entire range of observed earthquake magnitudes may be achieved by allowing coseismic slip to rupture to depths below the seismogenic layer.

Introduction

Classically, earthquakes have been characterized as a dislocation with average slip \bar{u} on a rectangular fault of width W and length L embedded in a homogeneous elastic half-space with rigidity μ , defining the seismic moment M_0 (equation 1). This dislocation results in an average stress drop $\Delta\tau$ on the fault plane (Kanamori and Anderson, 1975)

$$M_0 = \mu L W \bar{u}, \quad (1)$$

$$\Delta\tau = C \mu \frac{\bar{u}}{\mathcal{L}}, \quad (2)$$

where \mathcal{L} describes a characteristic length scale and C is a geometrical constant. It has been common practice since the work of Scholz (1982) to refer to the L and W models of earthquake behavior, whereby the length dimension \mathcal{L} is assigned the value L or W , respectively. Depending on which model is chosen, seismic moment is proportional to either LW^2 or L^2W :

$$M_0 = \alpha \mu L W^2, \quad W \text{ model}, \quad (3)$$

$$M_0 = \alpha \mu L^2 W, \quad L \text{ model}, \quad (4)$$

with $\alpha = \Delta\tau/C$, and for small earthquakes $L \approx W$, and hence $M_0 \propto \mathcal{L}^3$ (Scholz, 1997). There is a long lasting debate to which is a more correct description of the earthquake process and thus the physical origin of the interrelationship between M_0 , L , W , and α (Scholz, 1982; Romanowicz, 1992; Scholz, 1994; Bodin and Brune, 1996; Yin and Rog-

ers, 1996; Matsuura and Sato, 1997; Mai and Beroza, 2000; Shaw and Scholz, 2001; Miller, 2002) with important implications to seismic hazard (P. M. Mai *et al.*, unpublished manuscript, 2007). At the heart of the debate has been an aim to distill global mechanical dependencies beyond the complexity of individual earthquakes. Natural and synthetic area-moment scaling implies that the static stress drop of earthquakes of different magnitude is relatively constant (Kanamori and Anderson, 1975; Hanks, 1977; Wells and Coppersmith, 1994; Abercrombie, 1995; Ripperger *et al.*, 2007), which has led to the interpretation that earthquakes are self-similar. When the observation of constant stress drop is interpreted within the realm of elastic dislocation theory and the idea that coseismic slip is limited to the seismogenic layer, the observation of constant stress drop implies coseismic slip should scale with rupture width and thus ultimately saturate for ruptures of length dimension greater than the seismogenic thickness, W_s . However, observations relating slip (surface or on-fault) to rupture length L generally show that coseismic displacement \bar{u} continues to increase with L . The observations are thus in apparent conflict.

Discussing data by Scholz (1994), Shaw and Scholz (2001) posed a resolution to the apparent conflict through the numerical application of an elastodynamic model to show that the observed form of the coseismic slip versus length data could be explained with the application of scale invariant physics. Yet their results remained unsatisfactory when attempting to be explained in the context of a constant stress-drop model for earthquakes limited to the seismogenic layer—the frictional velocity-weakening part of the crust—of width W_s . Manighetti *et al.* (2007) have posed an alternate

explanation that asserts that large earthquakes are the result of the rupture of multiple discrete segments, each characterized by constant stress drop. Interestingly, examining the latter analysis of the empirical data reveals a tendency for values of rupture width to increase with rupture length. Liu-Zeng *et al.* (2005) argue that constant stress drop is not necessarily required to explain slip-length scaling. Based on the observation that slip of individual earthquakes is complex (e.g., Mai and Beroza, 2002), Liu-Zeng *et al.* (2005) demonstrate that heterogeneous fault slip produced by pulse-like models of earthquake rupture can play a key role in slip-length scaling. Miller (2002) explains \bar{u} - L data being controlled by the degree of overpressurization in a fault. In contrast to these models, empirical data do show that there is no apparent saturation of slip with L (Wesnousky, 2008).

Thus, the observation of continued slip with rupture length is in conflict with independent observations indicating earthquakes' stress drops are relatively constant and continues to pose a paradoxical situation. Specifically, the assumption that $W \leq W_s$ together with the increase in \bar{u} with L requires that large earthquakes have increasingly higher static stress drops than small events.

King and Wesnousky (2007) point out that because of depth-dependent spatial resolution problems neither geodesy (M. T. Page *et al.*, unpublished manuscript, 2007) nor seismology (Beresnev, 2003) have yet ruled out the possibility that large earthquakes do produce coseismic slip beneath the seismogenic layer ($W > W_s \approx 15$ km). They in turn showed that the stress-drop problem may be resolved by allowing coseismic slip to extend deeper into a zone with velocity-strengthening properties (Tse and Rice, 1986). While King

and Wesnousky (2007) examined the problem in terms of a static dislocation model, here we use quasidynamic simulations of spatiotemporal evolution of slip to examine the effect of relaxing the condition that slip be constrained to zero at the base of the seismogenic layer. Specifically, we concern ourselves with the interrelations between L , W , M_0 , \bar{u} , and $\Delta\tau$.

To do this synthetic seismicity is generated by a 3D quasidynamic rate-and-state controlled vertical strike-slip fault model with imposed heterogeneity of a governing frictional parameter (Fig. 1). Two frictional slip-rate-dependent profiles are used: (1) a boxlike (*b*) profile similar to the one used in previous studies (Tse and Rice, 1986; Rice, 1993; Lapusta *et al.*, 2000; Shibazaki, 2005; Hillers *et al.*, 2006, 2007), which confines the depth extension of earthquakes to 15 km, and (2) a profile with a steeper tapered (*t*) gradient below $z = -15$ km allowing accelerated slip associated with large events at greater depths while maintaining stable creep during interseismic periods (Fig. 2). Subsequent to briefly reviewing geological and seismological data bearing on the likelihood of a rate-dependent transition between stick-slip and stable sliding and the likelihood of coseismic slip beneath the seismogenic layer, we return to describe the models in more detail.

Structure of Shear Zones and Likelihood of Deep Slip

Mechanisms for deformation below continental strike-slip fault zones revolve around the end member cases of (1) distributed deformation in the lower crust and upper man-

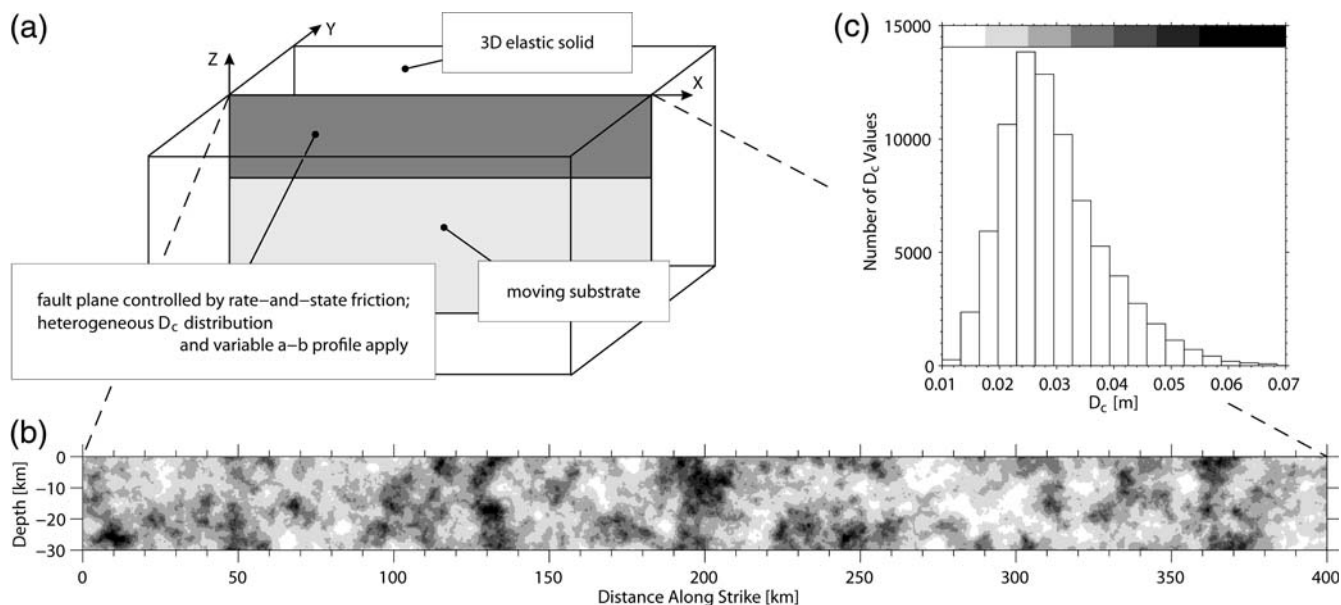


Figure 1. (a) Model geometry. (b) Example 2D D_c distribution with short (2 km) correlation lengths along strike and depth from a case with lowest resolution, R^l . $X = 400$ km, $Z = -30$ km, $n_x = 1024$, and $n_z = 78$. (c) Corresponding lognormal distribution of D_c values across the fault plane. This parameterization has been chosen to favor the occurrence of large events. See Hillers *et al.* (2007) for the role of D_c distributions as a tuning parameter.

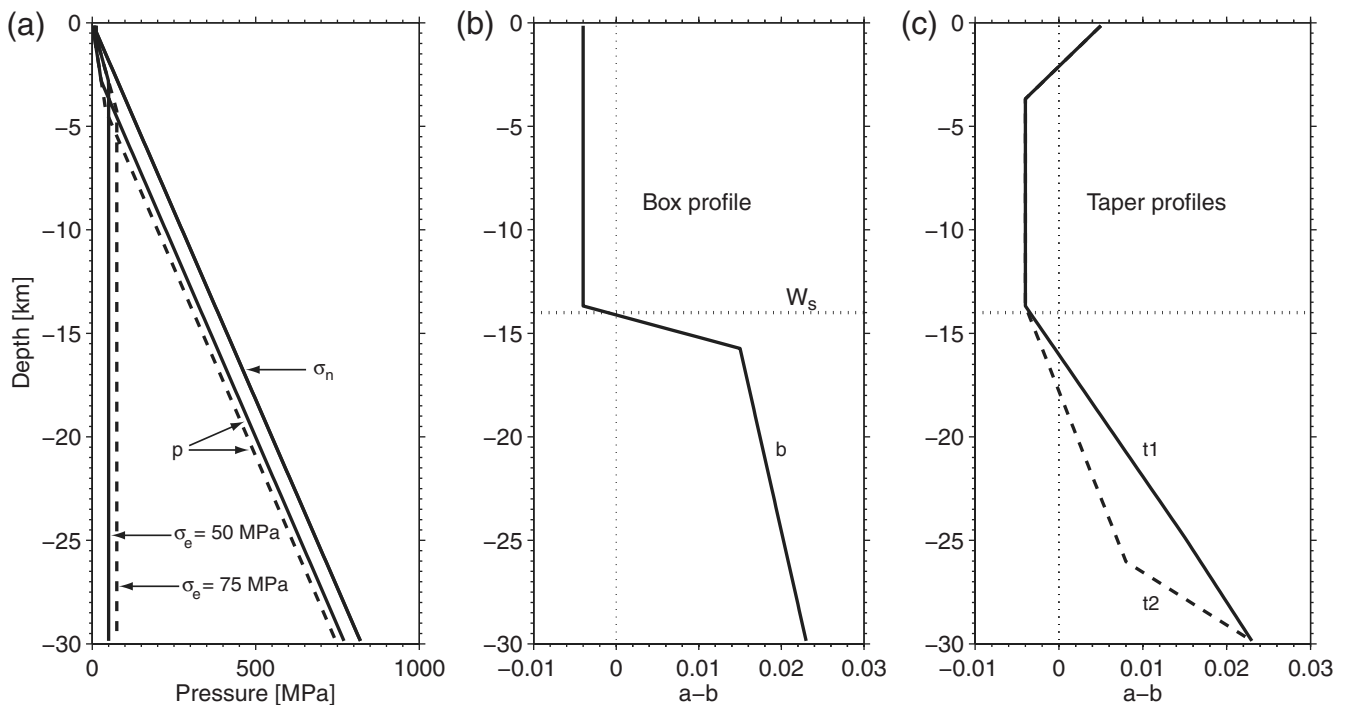


Figure 2. (a) Lithostatic normal stress (σ_n), pore pressure (p), and effective normal stress (σ_e). (b) Box (b) and (c) two tapered (t) $a-b$ profiles used throughout the study. Each $a-b$ profile (b , $t1$) is used respectively with a D_c map (e.g., Fig. 1b). The seismogenic width W_s is defined to be the deepest point where $a-b = -0.004 = \text{const}$, that is, $z = -14$ km.

tle and (2) deformation concentrated on faults that cut across the lower crust and mantle (e.g., Wilson *et al.*, 2004). Independent of structure, however, the brittle-ductile transition, the mineral-dependent peak in static crustal strength where Byerlee's law and the viscous, temperature- and strain-rate-dependent strength of the lower crust intersect, is assumed to coincide with the lower bound of crustal seismicity. In a quartzfeldspathic crust, the transition is usually interpreted as the onset of quartz plasticity at 300°C (~11 km), but feldspar shows plastic behavior at temperatures greater than 450°C (~22 km). Exhumed strike-slip faults with large offsets indicate a narrow zone of shear localization in fault cores exhibiting cataclastic and pseudotachylitic material (Chester and Chester, 1998; Passchier and Trouw 2005), whereas mylonites indicate narrow ductile shear zones at greater depths. Furthermore, the strength profile of mature strike-slip faults may have a much smaller strength gradient than the surrounding crust due to the presence of overpressurized fluids (Rice, 1992). Dynamic models including thermomechanical localization feedbacks also lead to significantly altered strength profiles in the lower crust (Regenauer-Lieb *et al.*, 2006). Regenauer-Lieb and Yuen (2007) argue that brittle-ductile coupling, leading to a midcrustal core supporting most of the crust's strength, offers new ways for understanding the root zone for large earthquakes, in contrast to purely frictional approaches. Discussing his now classic synoptic shear-zone model, Scholz (1988) states that large earthquakes can propagate into the regime where the quartz

response is viscous, but he allows the maximum width to be limited to the 15-km-depth range.

While distributed deformation is typical below strike-slip environments at plate boundaries in oceanic regions (Molnar *et al.*, 1999; Wilson *et al.*, 2004), there is ample evidence from exhumed faults that deep portions of strike-slip faults that undergo stable creep at low strain rates during interseismic periods show highly localized, rapid slip in response to high strain rates associated with downward propagating shear dislocations. By identifying brittily deformed feldspars within a ductily deformed quartz matrix in an exhumed section of a strike-slip fault corresponding to faulting depths of 15–20 km, Cole *et al.* (2007) modify Scholz's model by assuming an even broader semibrittle zone where coseismic localized slip and interseismic flow occur interchangeably (Sibson, 1980; Norris and Cooper, 2003). Observations and models of instantaneous deepening and subsequent shallowing of seismicity after a mainshock (Schaff *et al.*, 2002; Rolandone *et al.*, 2004; Ben-Zion and Lyakhovskiy, 2006) and variations in recurrence interval and moment of repeating aftershocks (Peng *et al.*, 2005) are further evidence that the base of the seismogenic layer reflects a rate-dependent transition between stick-slip and stable sliding.

It is thus reasonable to suggest that large earthquakes are likely to penetrate significantly deeper into the crust on localized slip horizons than the hitherto assumed width of the seismogenic layer, $W_s = 15$ km, associated with the occurrence of background seismicity.

Model Setup and Method

We use a friction-based approach to simplify more complex, brittle-ductile feedback mechanisms in the semibrittle transition zone at depth (Regenauer-Lieb *et al.*, 2006) to test the implication of deep coseismic slip on earthquake scaling relations. We use the 3D strike-slip fault model geometry discussed by Rice (1993) and Hillers *et al.* (2007), where a fault of $X = [400, 300, 200]$ km by $Z = -30$ km is discretized into $n_x = 1024$ by $n_z = [78, 102, 154]$ cells along strike and depth, respectively (Fig. 1), resulting in low, medium, and high resolutions R^l , R^m , and R^h , respectively. The fault is governed by the Dieterich–Ruina slowness rate-and-state formulation and is loaded by a substrate below 30-km depth moving with $v^\infty = 35$ mm/yr. This procedure greatly simplifies the numerical scheme. However, the implications of boundary conditions such as constant loading slip rate or driving stress imposed at vertical faces of a 3D crustal block, or distributed drag at the base of the crustal layer, may be considered in an alternative modeling approach. Governing equations and the numerical procedure can be found in Hillers (2006) and Hillers *et al.* (2007). We impose heterogeneous 2D distributions of the rate-and-state critical slip distance D_c on the frictional interface to prevent the system from generating only system-wide events rupturing the entire fault (Ben-Zion, 1996; Heimpel, 2003; Shaw, 2004; Zöller *et al.*, 2005).

To generate a database containing many large events, the degree of heterogeneity is chosen such that the system is allowed to produce big events more easily. Based on the results of Hillers *et al.* (2007), who investigated statistical properties of synthetic seismicity in response to D_c maps parameterizing different degrees and types of heterogeneity, we use log-normal distributions of D_c values across the fault with short correlation lengths along strike and depth (Fig. 1b,c). Using a default effective normal stress of $\sigma_e = 50$ MPa (Fig. 2a), minimum D_c values are chosen appropriately to perform simulations in the continuum limit.

Depth-Dependent Properties

Previous 2D antiplane (Tse and Rice, 1986; Lapusta *et al.*, 2000) and 3D (Rice, 1993; Shibazaki, 2005; Hillers *et al.*, 2006; Hillers and Miller, 2006, 2007) rate-and-state models of a strike-slip fault adopted a temperature- and hence depth-dependent a – b profile based on a geothermal gradient of the San Andreas fault (Stesky, 1975; Lachenbruch and Sass, 1980; Blanpied *et al.*, 1991). Tse and Rice (1986) demonstrated that this profile confines the occurrence of coseismic slip to about $z = -15$ km, and Scholz (1988) related the a – b rate dependence to the general structure of shear zones: Because of low normal stresses and the lack of hypocenters in this region, the topmost 3 km are usually interpreted to be velocity strengthening (Marone and Scholz, 1988; Marone *et al.*, 1991), parameterized by $a > b$. The lo-

calized slip zone between $-3 < z < -15$ km has constant velocity weakening, $a < b$, allowing instabilities to nucleate. Slip-rate dependence below this zone is again velocity strengthening and generally assumed to correlate with the onset of quartz plasticity.

The approach taken by Tse and Rice (1986) focuses on the interpretation of frictional data, neglecting complex rheological properties not captured by this parameterization. As they note, “Depending on rheology, the depth estimated for transition from unstable to stable frictional slip on a deeply penetrating crustal fault may or may not be the same.” Various other approaches that further incorporated complex rheological properties have also been examined. Chester (1995) and Shibazaki *et al.* (2002) have shown that the transition from unstable to stable slip is not necessarily abrupt or time independent.

To approximate the effect of different rheologies within the frictional framework, we vary the rate of change of a – b with depth, using two depth dependencies. The first shows an abrupt transition at 15-km depth whereas in the second the value a – b is taken to smoothly increase with depth below 15 km (Fig. 2b,c). The latter profile allows earthquakes to propagate significantly deeper, consistent with geological observations of exhumed mature faults. Following the slip-depth distributions of King and Wesnousky (2007), we compare scaling relations of events produced by these tapered distributions to properties of seismicity generated by the standard boxlike a – b profile that confines coseismic slip to about 15-km depth. To highlight the difference between box and taper models we use a constant a – b profile at shallow depths together with a relatively abrupt velocity-weakening to velocity-strengthening transition at 15-km depth for the

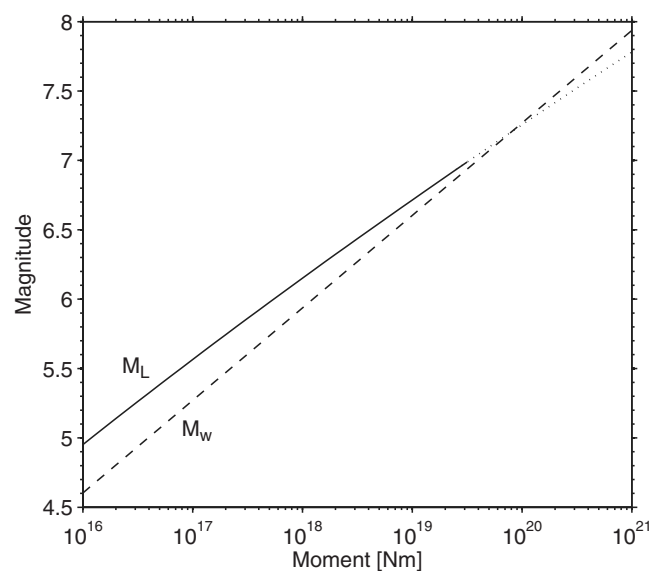


Figure 3. Local magnitude for Southern California M_L after Ben-Zion and Zhu (2002) and moment magnitude M_w after Kanamori (1977) versus seismic moment. The dotted segment of M_L indicates that M_L has been determined for $1 < M_L < 7$.

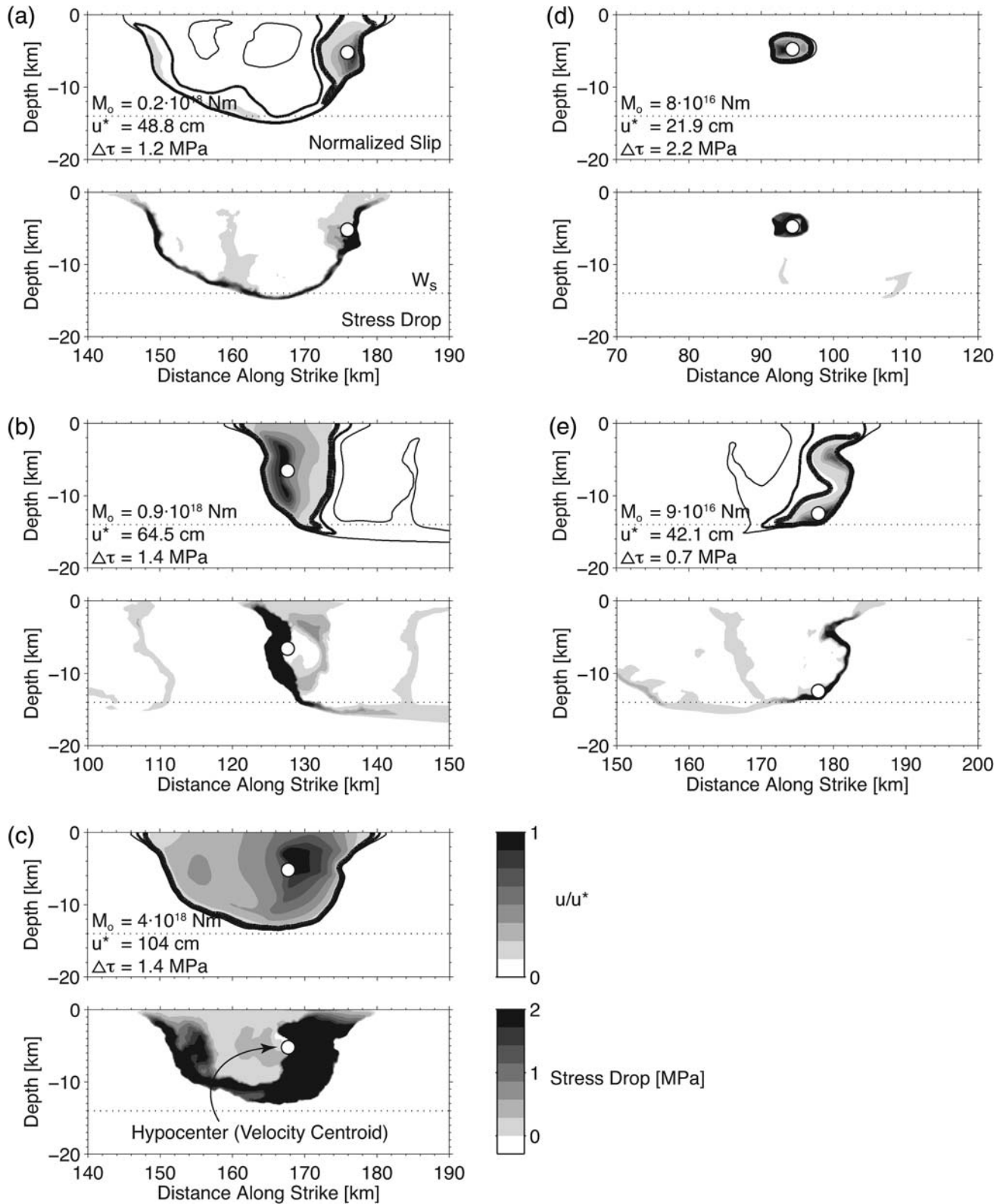


Figure 4. Example slip maps and corresponding stress change patterns produced by a box model (resolution R^h) to illustrate the saturation of W_s (a)–(c) and the origin of scatter in stress-drop values for small events (d) and (e), respectively. Contours of increasing thickness enclose areas of slip with [2, 5, 10]% of the maximum slip value, u^* . The heaviest line indicates the governing 10% of u^* contour. White circles denote hypocenters determined at the time of triggering within a circular region centered at the fastest slipping cell (Hillers *et al.*, 2007). (a)–(c): Because of the applied a – b profile, events with $M_0 > 5 \times 10^{18}$ N m (M_L 6.5, Fig. 3) propagate only along strike and mark the approximate transition between small and large events. (d) and (e): Slip and stress-drop distributions for two M_L 5.5 earthquakes, where $\Delta\tau$ differs about 300%. See Table 1 for detailed summary of event properties.

box models. We define the maximum depth extent of the velocity-weakening region where $a-b = -0.004 = \text{const}$ to be the width of the seismogenic zone, W_s .

Effective normal stress is chosen to be 50 MPa, $\sigma_e(z) = \sigma_n(z) - p(z)$, with $p(z) = \max[p_{\text{hyd}}(z), \sigma_{\text{lith}}(z) - 50 \text{ MPa}]$ (Fig. 2a). Considering elevated pore pressures within the fault zone alters the strength profile of crustal rocks associated with shear-zone models (Rice, 1992). While the strength profile of intact rock and/or dry friction follows the Byerlee envelope, mature faults fail under much smaller shear stresses. To test the significance of different degrees of overpressurization, we also conduct a set of simulations with an increased effective normal stress using $\sigma_e = 75 \text{ MPa}$, $X = 300 \text{ km}$, $nx = 1024$ (R^m), and a properly adjusted D_c value range.

Parameter Extraction

To extract slip events from the continuous stream of slip velocity, state, slip, and stress data generated during the numerical experiments, we use a slightly modified procedure

discussed by Hillers *et al.* (2006, 2007). We take the difference of slip and stress of all cells between event initiation—the velocity of the fastest slipping cell is larger than a trigger velocity v^{trs} , $v \geq v^{\text{trs}} = 10^4 v^\infty$ —and event termination—all cells have $v < v^{\text{trs}}$. We also monitor the maximum velocity of each cell during instabilities, $\hat{v}(x, z)$. These original $u(x, z)$, $\Delta\tau(x, z)$, and $\hat{v}(x, z)$ distributions are interpolated on a $50 \times 50 \text{ m}^2$ grid, allowing the investigation of different choices of the definition of I , the subset of cells that define the event. For example, we considered cells with \hat{v} and u being [1, 10]% of v^* and [2, 5, 10]% of u^* (the * denotes maximum values of an array/population), respectively, and find that these choices do not influence the overall conclusions presented here. Results discussed in the present study were obtained considering cells with $u_i \geq 10\%$ of u^* . Because of sometimes complex slip patterns consisting of multiple patches, we chose only the largest contiguous patch from each event, to reduce the “chance in the game of determining slip and length of an event” (Liu-Zeng *et al.*, 2005). The dimensions L and W of those patches have been determined, as well as the mean slip \bar{u} and mean stress drop

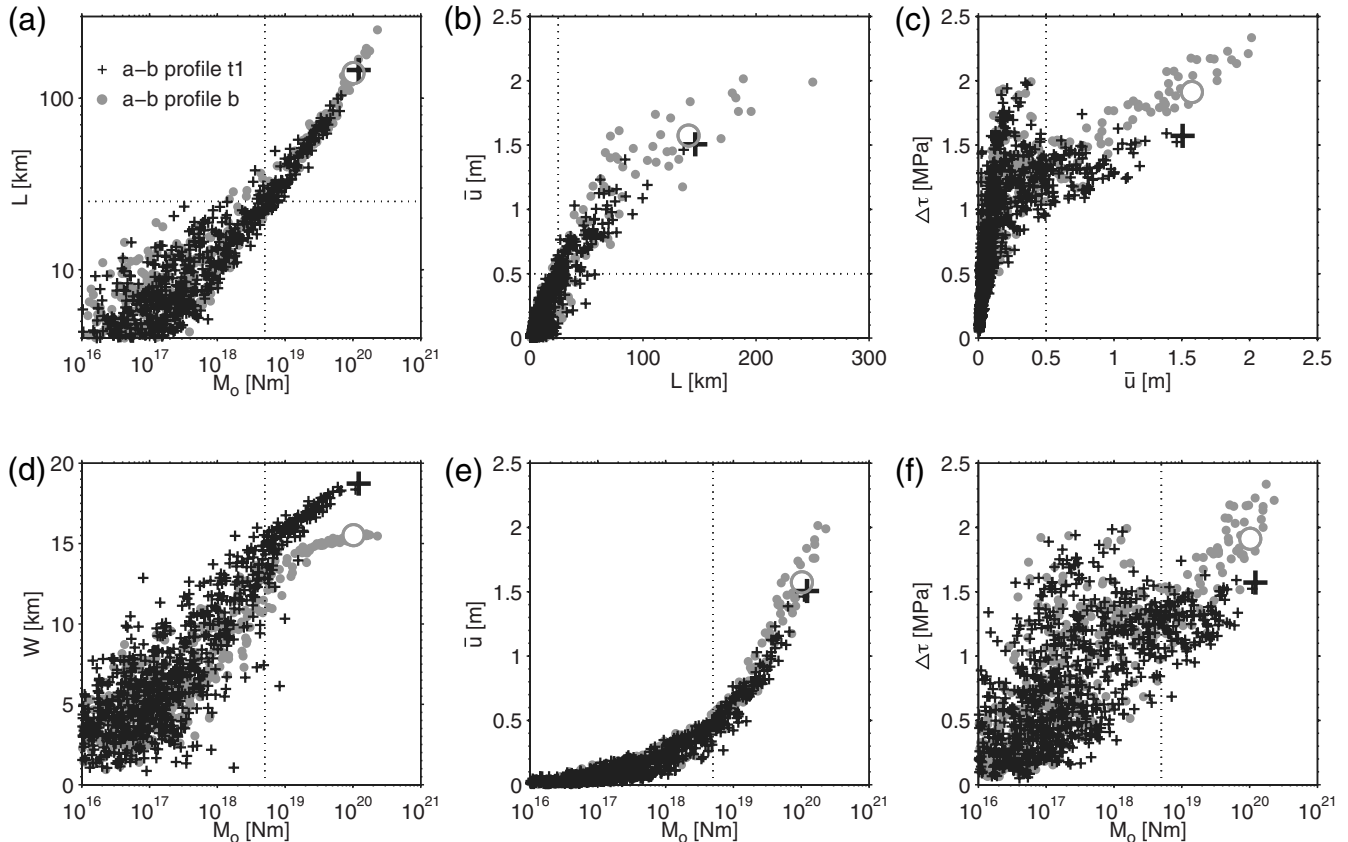


Figure 5. Scaling relations of a box and taper model with $\sigma_e = 50 \text{ MPa}$, $v^{\text{trs}} = 10^4 v^\infty$, R^m . (a) Length-moment, (b) slip-length, (c) stress-drop-slip, (d) width-moment, (e) slip-moment, and (f) stress-drop-moment scaling. Here and in all subsequent scaling figures, if not specified otherwise: taper model, black plus signs; box model, gray circles. Dotted horizontal and vertical lines separate small from large events (Fig. 4). Highlighted symbols denote events discussed in Figure 7. Key results: (a) Events from the box and taper populations with similar moments cannot be distinguished by their lengths; (b) nonlinear \bar{u} - L scaling as discussed in King and Wesnousky (2007); (d) relaxed a - b profiles below W_s result in increased widths of taper events; (e) for large events, $\Delta\tau$ of box events scales with M_0 , in contrast to observations, whereas the stress drop of taper events does not scale with event size.

$\Delta\tau$. To estimate the event size in terms of seismological observables, we compute the seismic potency $P_i = a \sum_{i \in I} u_i$ or $P = LW\bar{u} = A\bar{u}$ (Ben-Zion, 2003), with a being the area of a cell, and $M_0 = \mu P_i$, where $\mu = 30$ GPa. Figure 3 illustrates the relation between M_0 and a local magnitude for southern California earthquakes ($1 < M_L < 7$) (Ben-Zion and Zhu, 2002) and moment magnitude M_w (Kanamori, 1977).

While it is desirable to explore scaling relations up to very large earthquakes (M 8), the largest magnitudes generated by our simulations are about M 7.5. A typical M 7.5 event from the box model has $W = 15$ km, $L = 250$ km, and $\bar{u} = 220$ cm, which leads to $P = 8.3 \times 10^5$ km² cm. The corresponding potency of an M 8 event is $P = 10^7$ km² cm, which requires $W = 15$ km, $L = 670$ km, and $\bar{u} = 10$ m. The dimensions and resolutions necessary to produce (several) model earthquakes of this size are at present computationally too cumbersome.

Analysis

Slip and Stress-Drop Distributions of Typical Events

Figure 4a–c shows some typical slip and corresponding stress-drop distributions for events with $M_0 \approx [0.2, 1, 5] \times 10^{18}$ N m generated by a high-resolution box model. Figure 4a,b,e demonstrates the effect of differing the values of defining limits I , using thresholds of [2, 5, 10]% of u^* . While the effect is largest for small events because u^* is relatively small here, the choice of the threshold is less significant for events with $M_0 > 5 \times 10^{18}$ N m. This is illustrated by the close proximity of the contours for the larger event (Fig. 4c) compared to the significantly different contour pattern shown in Figure 4a. Figure 4c shows an event where W_b reaches the width of the seismogenic zone, W_s . Hence, in our analysis, we will focus on large events with moments above that threshold, corresponding to M_L 6.5 and M_w 6.4, respectively (Fig. 3).

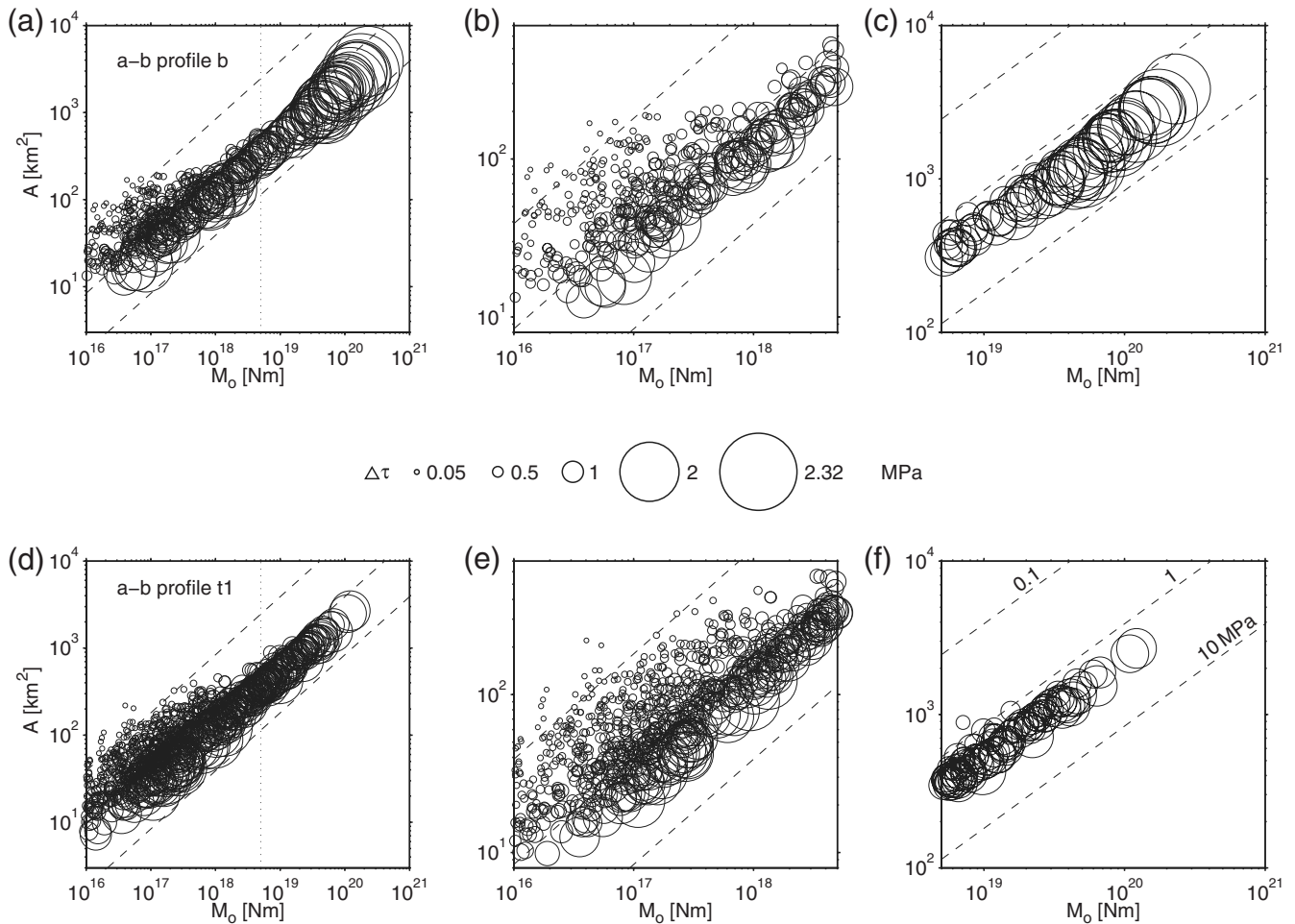


Figure 6. Area-moment scaling with $A = A_i = \sum_{i \in I} a_i$. Top: Data from box model (Fig. 5, gray symbols). Bottom: Data from taper model (Fig. 5, black symbols). (a) and (d) Entire magnitude range. (b) and (e) Subset of (a) and (d), A – M_0 scaling for small events. (c) and (f) Subset of (a) and (d), A – M_0 scaling for large events. Broken lines denote theoretical estimates of constant stress drop. Note that for profile $t1$, $\Delta\tau$ of individual events, symbolized by the circle size, follows the constant theoretical estimates for large events, whereas for profile b the measured stress drops increase with increasing moment.

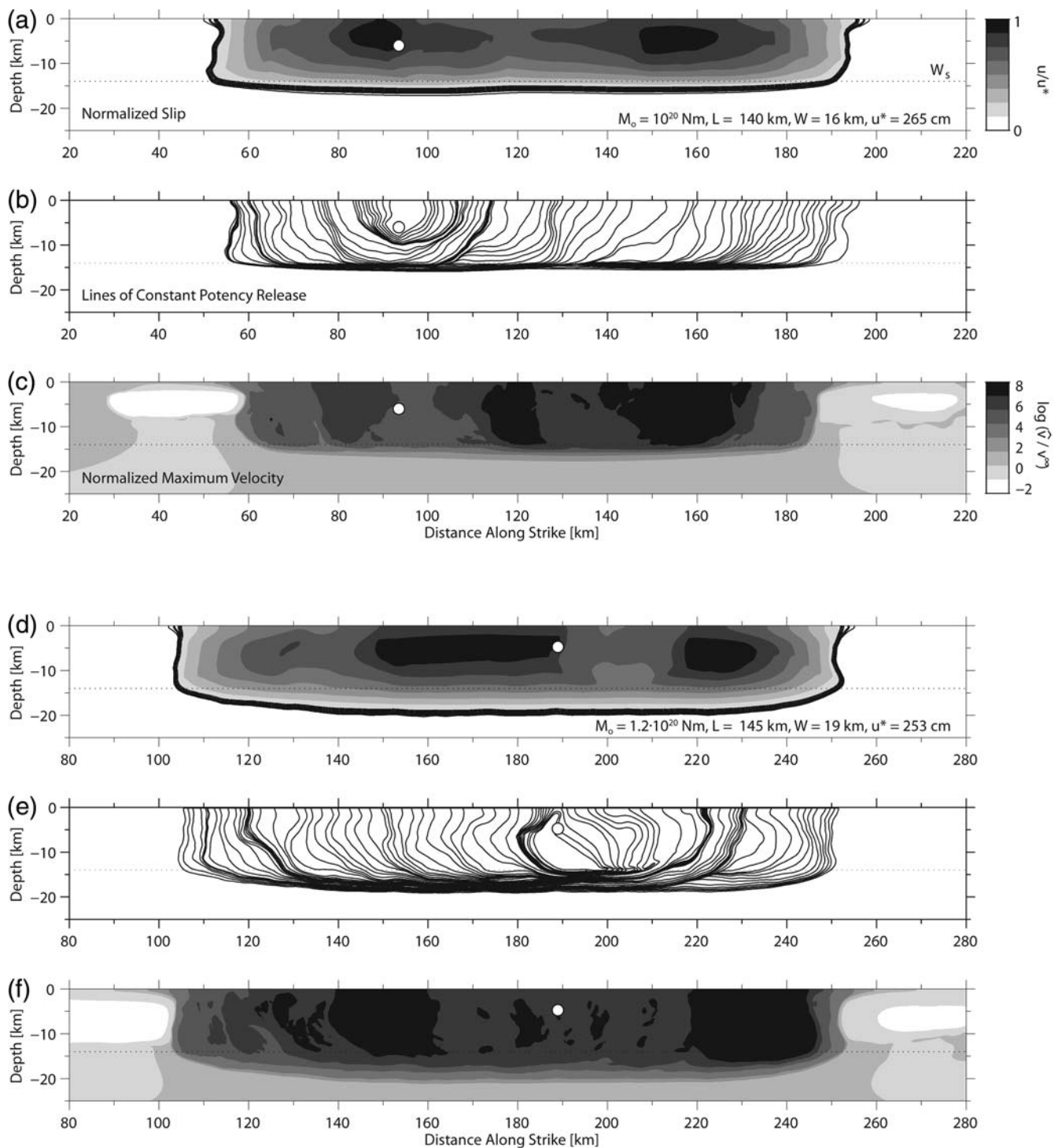


Figure 7. Comparison of two respective M_L 7.3 events (highlighted in Fig. 5) from the (a)–(c) box and (d)–(f) taper model, R^m , with $L_b \approx L_t$ and $M_{0b} \approx M_{0t}$. (a) and (d) Final slip distributions. (b) and (e) Contours of constant potency release. (First 10 contours are plotted at a five times higher rate than subsequent contours.) Note the difference in upward propagation at early stages due to $a > b$ versus $a < b$ in the topmost part of the box and taper model, respectively (Fig. 2). (c) and (f) Distributions of maximum slip-rate values during the events, scaled to the load velocity v^∞ . The growth and velocity images of the taper event (e) and (f) suggest that growth rates and to a lesser extent slip rates below W_s are smaller compared to values in the seismogenic zone. However, moment release above/below W_s is 87%/13% in the taper model, compared to 97%/3% in the box model. See Table 1 for detailed summary of event properties.

Table 1
Source Parameters for Events Discussed in Figures 4 and 7

Model	Figure	M_L	$M_0(\text{N m})$	$\sum_{i \in I} a_i (\text{km}^2)$	$P_i (\text{km}^2 \text{ cm})$	$L(\text{km})$	$W(\text{km})$	$A(\text{km}^2)$	$\bar{u}(\text{cm})$	$u^*(\text{cm})$	$P[\text{km}^2 \text{ cm}]$	$\Delta\tau(\text{MPa})$	$\tau^*(\text{MPa})$
R^h , box	4a	5.73	1.93×10^{17}	46.8	6.423×10^2	4.2	6.6	27.8	13.7	48.8	3.814×10^2	1.2	11.8
	4b	6.12	8.67×10^{17}	116.4	2.889×10^3	8.5	9.6	82.3	24.8	64.5	2.044×10^3	1.4	10.4
	4c	6.49	3.95×10^{18}	289.3	1.315×10^4	22.9	10.4	237.5	45.5	104.0	1.079×10^4	1.4	11.8
	4d	5.51	8.17×10^{16}	16.8	2.722×10^2	4.9	3.3	16.2	16.2	42.1	2.624×10^2	2.2	11.6
	4e	5.54	9.25×10^{16}	54.9	3.085×10^2	4.6	4.5	20.5	5.6	21.9	1.150×10^2	0.7	7.2
R^m , box	7a–c	7.26	1.02×10^{20}	2163.2	3.406×10^5	140.3	15.5	2177.1	157.5	264.9	3.428×10^5	1.9	12.8
R^m , taper $t1$	7d–f	7.30	1.21×10^{20}	2669.9	4.019×10^5	146.2	18.6	2715.6	150.5	253.3	4.087×10^5	1.6	10.3

The exact area $A_i = \sum_{i \in I} a_i$ is obtained considering individual cells in the subset I , with a being the cell size, while A is the product of the averaged values W and L . P_i and P are the corresponding potency values. Differences between A_i , A and P_i , P are due to complex shapes—dominating the estimates for small events.

Figure 4d,e shows two example stress change distributions of small events to illustrate the origin of scatter for small moments in subsequently discussed scaling relations. Small compact shapes (Fig. 4d) result in stress drops that are in the range of the constant $\Delta\tau_i$ level for larger events. Irregular shapes (Fig. 4e) obtained by the same event-extraction algorithm result in lower average stress drop. Small $\Delta\tau$ values for small earthquakes are a result of the heterogeneous boundary conditions and of the quasidynamic approximation, because maximum slip rates are considerably smaller ($v^* \approx v^{\text{trs}}$) than for large events ($v^* \gg v^{\text{trs}}$). In tandem with the relatively coarse resolution and the event-extraction method, this leads to stress drops that underestimate observed values. Strictly speaking, these events are not mature slip events, but instabilities that are frustrated at early stages when slip rates have not become really dynamic yet.

Main Result

Figure 5 shows a compilation of scaling relations between L , W , M_0 , \bar{u} , and $\Delta\tau$ obtained from a typical box and taper model with medium resolution (R^m). As explained, data for small events ($M_w < 6.4$) show considerable scatter, whereas data for event sizes with $W \geq W_s$ do not.

Spatial Dimension, L and W (Fig. 5a,d). Both box and taper models show identical L – M_0 scaling, that is, similar rupture lengths (which are most easy to determine for real ruptures) result in seismic moments of comparable size. For this reason, it is unlikely that empirical observations of moment versus length, either rupture length (Wells and Coppersmith 1994) or the length of aftershock zones (e.g., Kagan, 2002), are sufficient to lend any insight to the depth extent of earthquakes. Because taper a – b profiles allow ruptures to release strain energy by propagating deeper, rupture length as a function of moment tends to be larger for box events than taper events; hence, $L_b^* > L_t^*$. We observe a break in L_b – M_{0b} scaling at $M_0 \approx 2 \times 10^{19}$ N m ($M_w \approx 6.6$), suggesting a breakdown of self-similarity associated with the saturation of W_s , that is, box ruptures tend to grow exclusively in the along-strike direction. The few data points for the taper model make it difficult to infer the same dependence. Rupture width W_b reaches a maximum at about $M_0 \approx 2 \times 10^{19}$ N m, due to the imposed a – b profile prohibiting unstable slip below $z = -15$ km. The tapered a – b profiles allows W_t to grow with increasing L , and to level off at greater depths, depending on the gradient of the profile (see the following discussion).

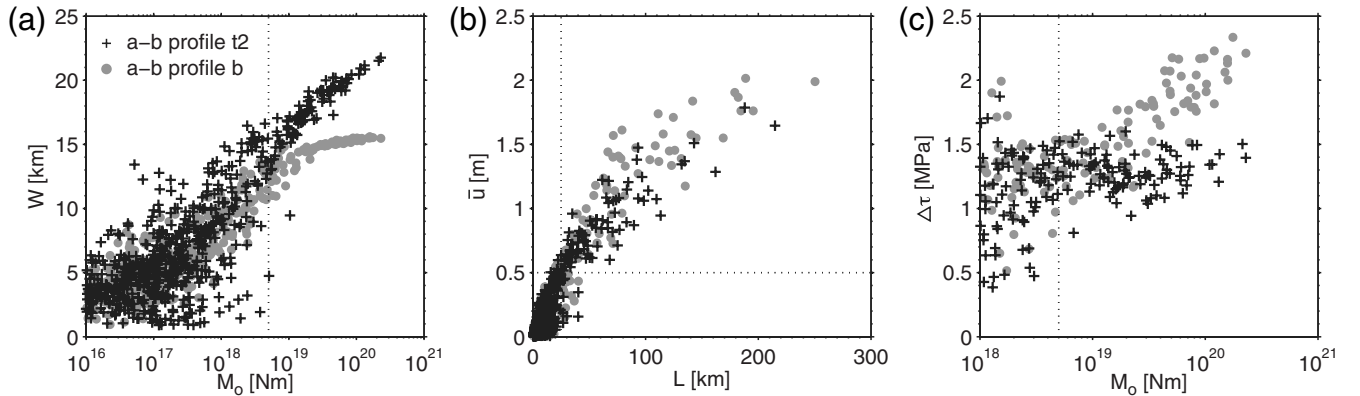


Figure 8. Effect of steeper a – b taper gradient (profile $t2$, Fig. 2c), R^m . (a) Width–moment, (b) slip–length, and (c) stress–drop–moment scaling. Box data (gray) as in Figure 5. Note the increased widths of large events compared to the data produced with the $t1$ profile (Fig. 5, black data), and the resulting clearer separation of $\Delta\tau$ – M_0 data at large magnitudes.

Slip (Fig. 5b,c,e). Slip-length scaling is at the heart of the problem whether $\Delta\tau$ is expected to be constant or not. Our synthetic data up to $L_b = 250$ km suggests a continuous increase with slip, but decreasing growth rate, consistent with King and Wesnousky (2007). Mean slip of large taper events, \bar{u}_t , tends to be less than corresponding \bar{u}_b , because the area of taper events is systematically larger, maintaining the observed constant L - M_0 scaling.

Stress Drop (Fig. 5c,f). The most significant result is the increase of $\Delta\tau$ with \bar{u} and M_0 for box events, whereas large earthquakes from taper models do not show an increase of $\Delta\tau$ with \bar{u} or M_0 . Only at the largest moments where W_t begins to saturate, data points allow an orientation toward larger $\Delta\tau$ values. Hence, the continued downward propagation of taper events leads to constant stress drops for large events, compatible with seismic observations. Furthermore, identical L_t - and L_b - M_0 scaling suggest that differences in scaling behavior cannot be detected by length measurements, but depend on an accurate estimate of the rupture's depth extension.

Area Moment. Figure 6 shows the corresponding area-moment scaling of the box and taper model discussed in Fig-

ure 5. At first order, the bulk of data follows the expected linear relation on a double logarithmic scale associated with a classic constant stress-drop model. However, interesting deviations from this global trend are as follows:

(1) In both cases, $\Delta\tau$ of small earthquakes (Fig. 6b,e) increase with smaller A (here, $A = A_i = \sum_{i \in I} a_i$) for constant M_0 following the theoretical lines of constant stress drop (Fig. 6b,e), consistent with dislocation theory, because for $\bar{u}_1 = \bar{u}_2$ and $A_1 < A_2$ follows $\Delta\tau_1 > \Delta\tau_2$.

(2) The increase in circle size illustrates the increase in $\Delta\tau$ for box-model events with increasing moment that is not observed in the taper model (Fig. 6c,f, as in Fig. 5f). That is, earthquakes with $W > W_s$ produce scaling relations that are fully compatible with observed A - M_0 relations and theoretical constant $\Delta\tau$ considerations, in contrast to slip events with $W = W_s$.

Comparison of Two Large Box and Taper Events with Similar Magnitude

Figure 7a,d shows final slip distributions of two events with comparable moments from the previously discussed box and taper event populations (R^m), respectively, illustrating the origin of the discussed differences in scaling relations for large earthquakes. Data for these particular earthquakes

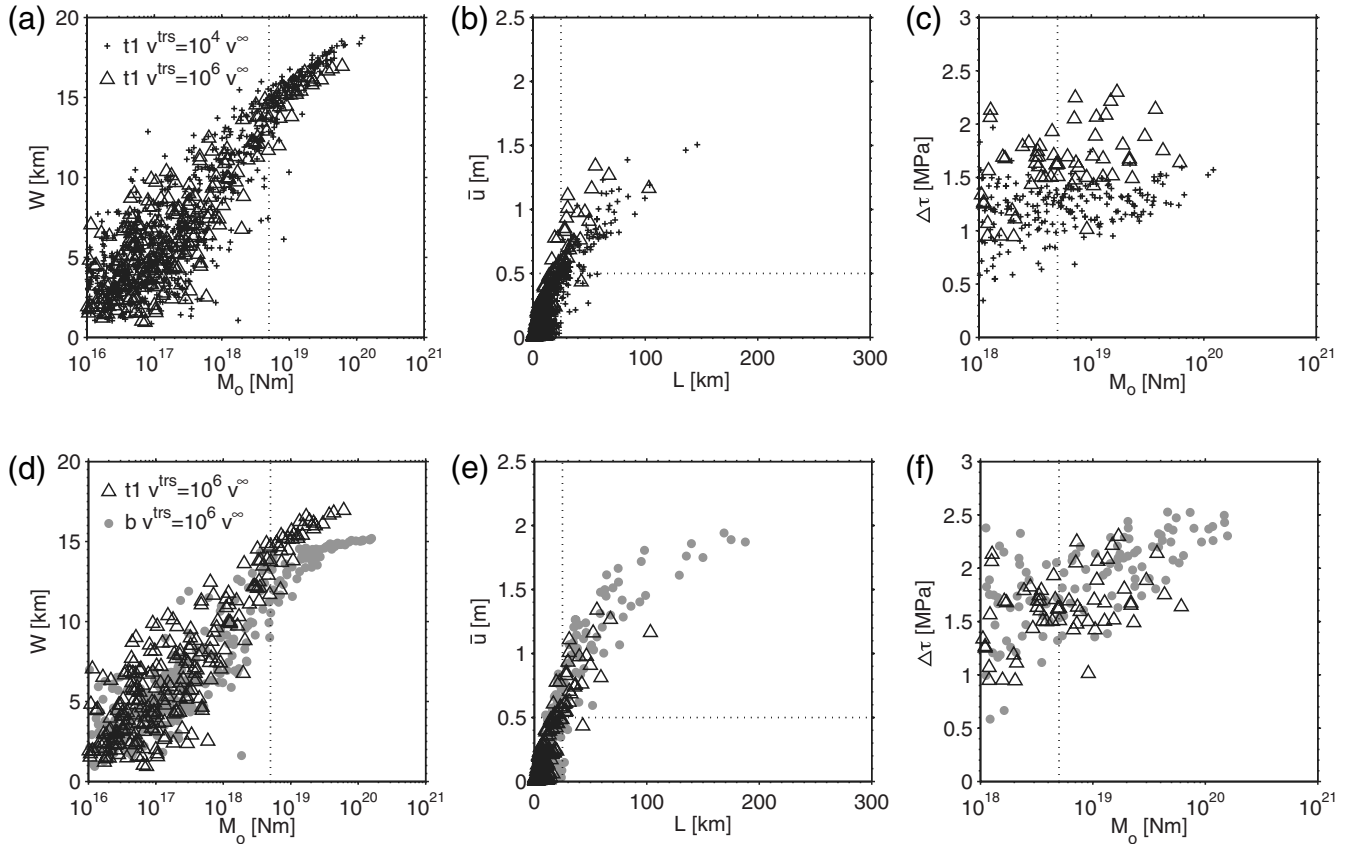


Figure 9. Effect of different trigger threshold, v^{trs} . (a)–(c) Scaling relations of two taper models with $v^{\text{trs}} = 10^4 v^\infty$ (plus signs, as in Fig. 5) and $v^{\text{trs}} = 10^6 v^\infty$. R^m . Most significant is the constant shift in $\Delta\tau$ - M_0 scaling. (d)–(f) Comparison of box and taper event populations, both with $v^{\text{trs}} = 10^6 v^\infty$, R^m . Triangles as in (a)–(c).

are marked by the enlarged plus signs and circles, respectively, throughout Figure 5. Table 1 gives a complete overview of the inferred parameters, showing that both lengths and moments are approximately the same. Because of different a - b dependencies at depth, W_t is 20% larger than W_b , but the mean slip for this pair is of comparable size (8% difference). Consequently, the box event has more slip on a smaller area and thus about 20% larger average stress drop than the taper event. Slip below W_s of the box event contributes only 3% to the total moment, in contrast to the 13% seismic moment release by the taper event.

The corresponding figures showing potency release contours (Fig. 7b,e) reveal the effect of the abrupt a - b transition of the box model: slip associated with the instability does not propagate below $z \approx -16$ km and continues to grow only laterally after the event has reached about one-third its final length. The taper event shows a different behavior: slip accumulates continuously along strike and depth, but with significantly reduced growth rates and slip velocities at depth. The relative decrease in rupture speed and slip rate below the seismogenic layer for the taper model suggests that combined inversions of high- and low-frequency bands are necessary to resolve the actual amount of moment release.

The systematic increase in depth and slip with L cannot be explained solely by a pulse (W) model but requires there be some continued slip behind the propagating rupture front. Similarly, the relaxation of a maximum rupture width $W^* \geq W_s$ violates the fundamental L -model assumption. Hence, the behavior exhibited by taper-model earthquakes can at best be described by a hybrid L - W scaling behavior, demonstrating that neither L or W exclusively control the final size of an instability. Maximum slip velocities during the box event show a sharp transition around W_s (Fig. 7c), whereas increased velocities of the taper event are tapered below $z = -14$ km (Fig. 7f).

Effect of Steeper a - b Gradient t_2

A steeper gradient t_2 in Figure 2c affects W_t - M_0 scaling most significantly (Fig. 8a), allowing ruptures to propagate deeper compared to the t_1 gradient. Note that the maximum width using t_2 is about $W_{t_2}^* = 22$ km, whereas $W_{t_1}^* = 19$ km (Fig. 5d). This increase in rupture area confirms that average slip generated by taper models is less than the slip of box models (Fig. 8b). Furthermore, gradient t_2 leads to $M_{0t}^* \approx M_{0b}^*$, showing no increase of $\Delta\tau_t$ at largest event sizes (Fig. 8c), verifying the separation in stress-drop

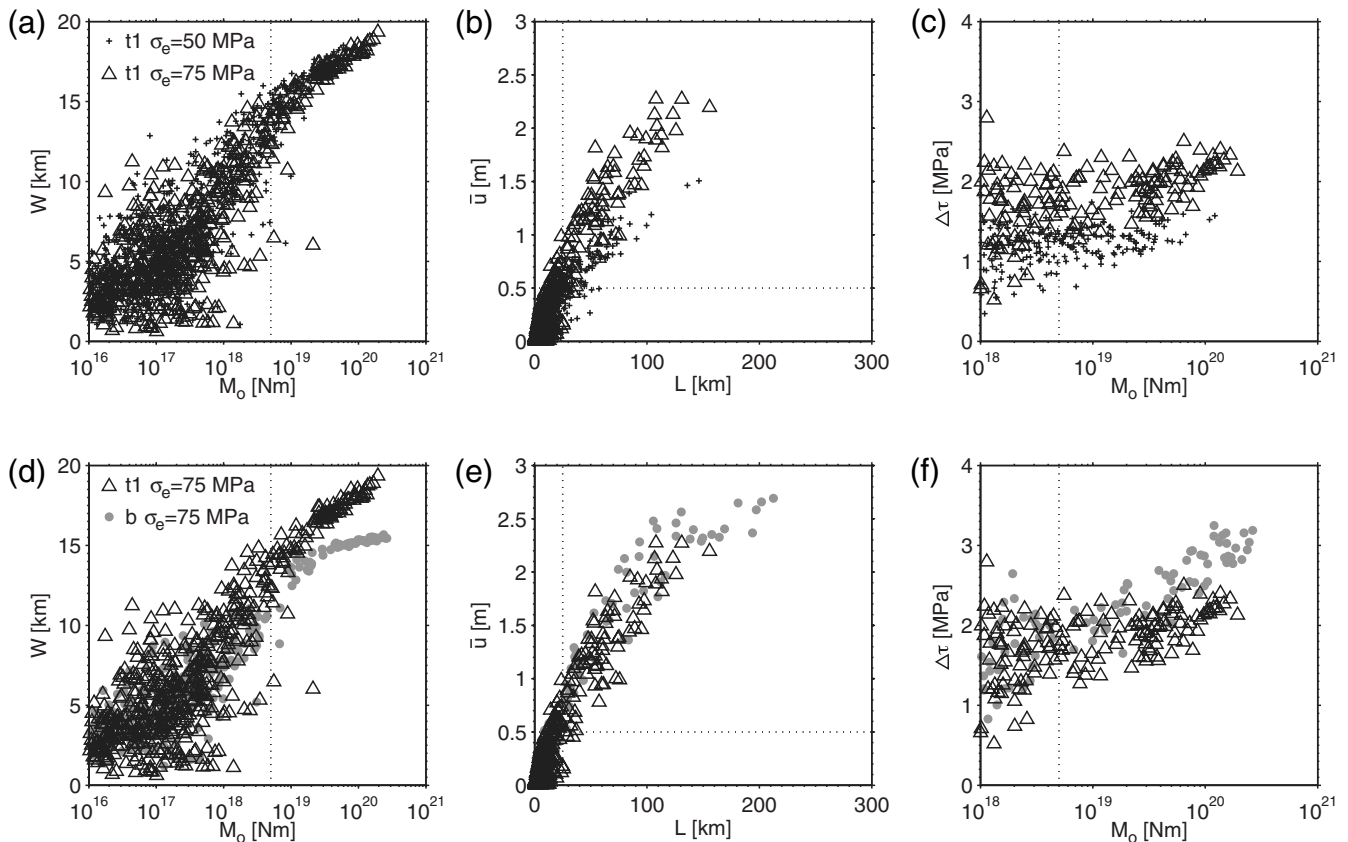


Figure 10. Effect of different normal stress σ_e (Fig. 2a). (a)–(c) Scaling relations of two taper models with $\sigma_e = 50$ MPa (plus signs, as in Figs. 5 and 9a–c) and $\sigma_e = 75$ MPa, R^m . Most significant is the large increase in coseismic slip occurring on the stronger fault and the associated constant shift in $\Delta\tau$ - M_0 scaling. (d)–(f) Comparison of box and taper event population, both with $\sigma_e = 75$ MPa, R^m . Triangles as in (a)–(c).

scaling between taper and box event populations. Or, more specifically, the lack of dependence of stress drop on rupture length for large earthquakes.

for large events do not change (Fig. 7), \bar{u} scaling remains unaffected, and the $\Delta\tau$ scatter at small events is reduced together with a slight decrease of the overall $\Delta\tau$ level.

Effect of Event Size Threshold

Using a smaller relative slip threshold (percentage of u^*) leads to a larger subset I , increasing the number of cells with small slip values (Fig. 4a). Hence, the scatter in W and L increases for small events, but the corresponding estimates

Effect of Trigger Threshold

A larger trigger threshold $v^{\text{trs}} = 10^6 v^\infty$ instead of $v^{\text{trs}} = 10^4 v^\infty$ decreases the number of cells belonging to a given event. Due to the localized acceleration at event nucleation, the consideration of slip accumulated with

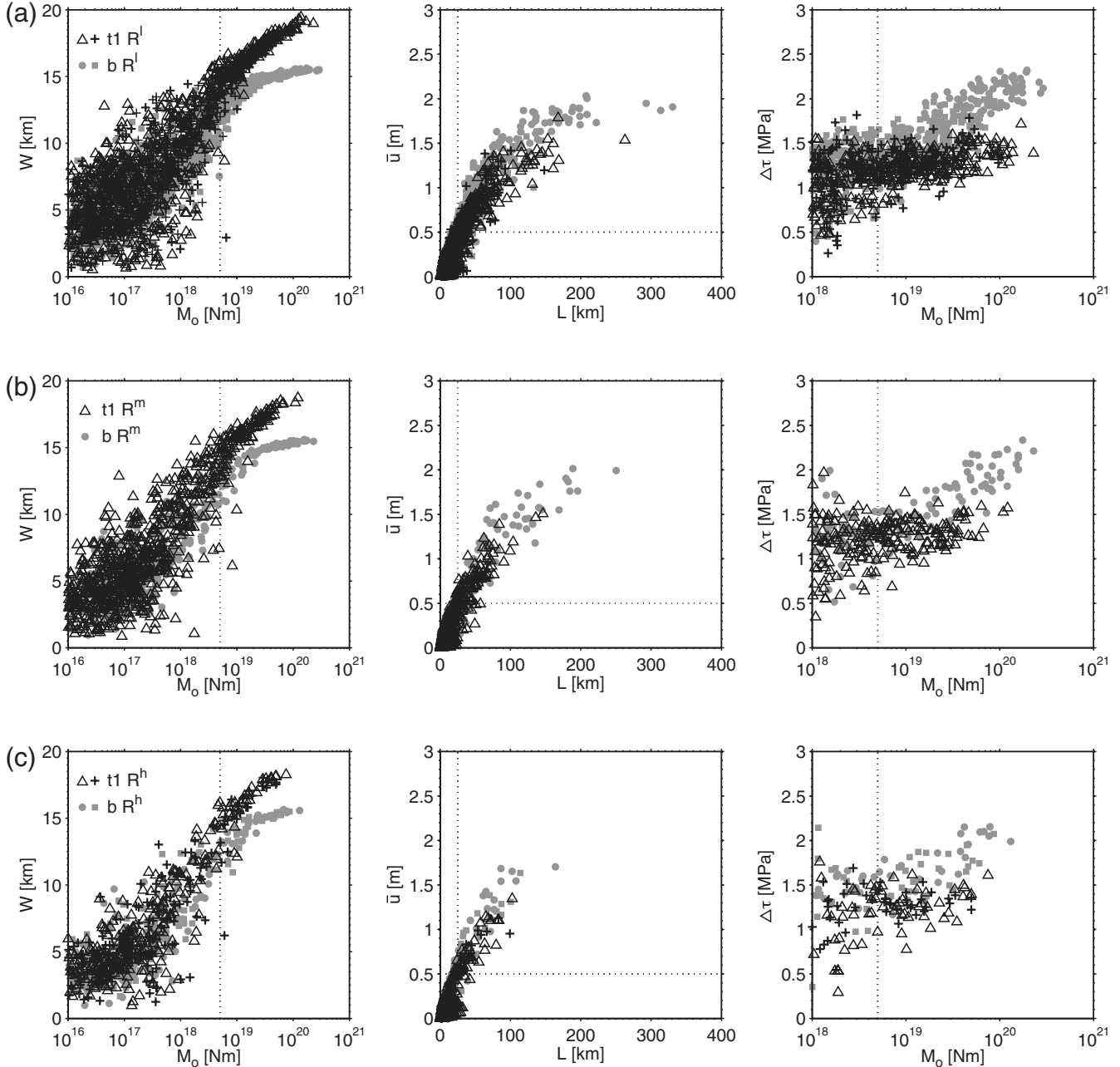


Figure 11. Effect of compliance ($X/nx \rightarrow \min[D_c]$). (a) Low resolution R^l . Event with largest moment in W_l-M_{0l} scaling corresponds to the $L_l = 263$ km event in \bar{u}_l-L_l scaling. Note the saturation of its width. (b) Medium resolution R^m . (c) High resolution R^h . The longest R^l models produce the largest synthetic earthquakes. The overall similarity of the scaling relations among the three cases suggests the first-order results are insensitive to resolution and hence robust features of the physical parameterization.

lower slip rates corresponds exclusively to the inclusion of afterslip-like displacement, which takes place at the edges of the fault (Fig. 7c,f). Hence, taper events do not reach as deep as using the default v^{trs} value (Fig. 9a), which results in a decrease in rupture area. Similar displacements (Fig. 9b) on a reduced area lead to a resulting higher but still constant $\Delta\tau$ level (Fig. 9c). With a larger v^{trs} value the differences between taper and box scaling (Fig. 9d–f) are less pronounced. While the widths for large events still belong to different populations, the \bar{u} – L scaling suggests only a weak trend of separation. The $\Delta\tau$ – M_0 data are less significantly separated, although the increasing and constant trend in the box and taper models, respectively, is observable. Differences in stress-drop behavior between the two datasets can be detected only for the largest events.

Effect of Normal Stress

To investigate the impact of different effective normal-stress conditions, we compare a box and taper model set with $\sigma_e = 75$ MPa to the set using the default value of $\sigma_e = 50$ MPa (R^m). Figure 10a–c compares the results of two taper models with different pore pressure profiles. While the W – M_0 scaling with $\sigma_e = 75$ MPa shows slightly smaller widths for the same moment (Fig. 10a), coseismic displacements tend to be significantly larger than for $\sigma_e = 50$ MPa (Fig. 10b). Consequently, $\Delta\tau$ values are at a higher level but exhibit the same constant trend (Fig. 10c). Increased fault strength leads to larger slip deficits and in turn to increasing coseismic-slip values and a reduced seismicity rate.

Scaling relations of box and taper models with $\sigma_e = 75$ MPa (Fig. 10d–f) show the previously established features, where a separation of \bar{u} – L data from the two models occurs at larger L values (100 km) compared to the $\sigma_e = 50$ MPa case (Fig. 5b, 75 km). Stress drops $\Delta\tau_t$ for large M_{0t} tend to increase because of larger displacements at associated widths compared to $\sigma_e = 50$ MPa (Fig. 10f).

Effect of Resolution—Compliance

It is expected that a higher spatiotemporal resolution (allowing to use smaller D_c values) leads to a more pronounced difference between the box and taper case, similar to the use of a steeper taper gradient discussed in Figure 8. However, the limited spatial dimension $X = 200$ km for R^h (Fig. 11c) leads to rupture lengths and, hence, maximum event sizes that are about half a magnitude smaller than for the R^l case (Fig. 11a). Nevertheless, the following trends can be extracted: (1) The resolution does not affect the maximum depth extension, W^* (Fig. 11, left). (2) The separation of \bar{u} – L populations becomes effective at smaller lengths for more compliant grids (Fig. 11, center). (3) Consequently, differences of the stress-drop levels at the transition between small and large events become more pronounced the higher the resolution (Fig. 11, right).

These trends can be attributed to the compliance of the grid, the associated choice of minimum D_c , and the resulting

slip-rate dependence with size (Fig. 12). Small events produced by low-resolution models have larger velocities because larger regions have to become unstable to reach the trigger threshold. Stiffer numerical grids lead to consistently smaller slip velocities v^* during medium sized slip events. These differences do not persist at large, fully developed instabilities.

The data for large L in the \bar{u} – L scaling Figure 11a ($L_b \approx 300$ km, $L_t \approx 260$ km) suggest a final saturation of \bar{u} for large events, most visible for the box case. This can readily be explained by the saturation of W at about W_s . But even in the taper case, the largest event saturates at the maximum depth allowed by the applied a – b profile (Fig. 11a, W – M_0 scaling). Hence, saturation of \bar{u} for large L is demonstrated to be associated with the saturation of W . The lack of available data suggesting this behavior for natural seismicity thus supports the hypothesis made in this study.

Slip-Depth and Hypocenter-Depth Distributions

Slip-depth distributions further illustrate the effect of spatiotemporal resolution (Fig. 13). On average, large ($M > 7$) earthquakes accumulate more slip the better the resolution but cease at identical depths (Fig. 13a,c). Slip in box events is consistently larger than in taper events (Fig. 5b), while for the latter slip horizons propagate significantly deeper (Figs. 5d, 8a, 9d, 10d, and 11, left), leading to a significant difference in moment partition between above and below W_s , respectively (see figure captions for details).

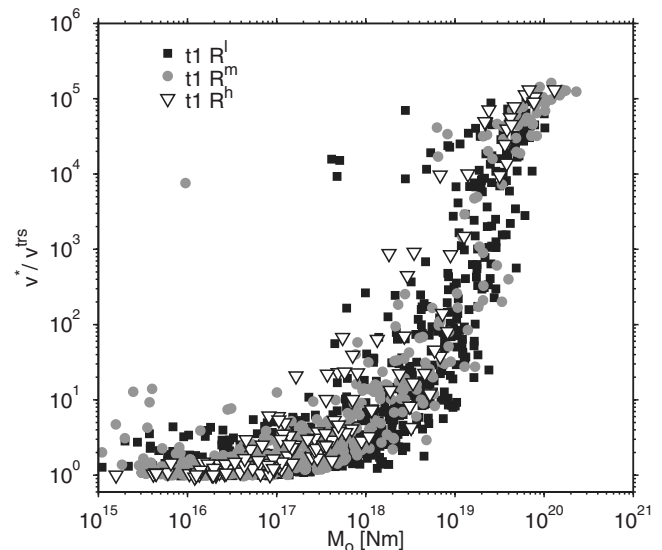


Figure 12. Effect of compliance on maximum velocity v^* . Small instabilities produced by less compliant models have larger velocities because larger regions have to accelerate, as a consequence of the $\min[D_c]$ -dependent nucleation size. Medium sized events from high-resolution simulations show larger velocities, because smaller regions can become more unstable. Data from all resolutions merge at large magnitudes. $v^{\text{trs}} = 10^4 v^\infty$, $\sigma_e = 50$ MPa.

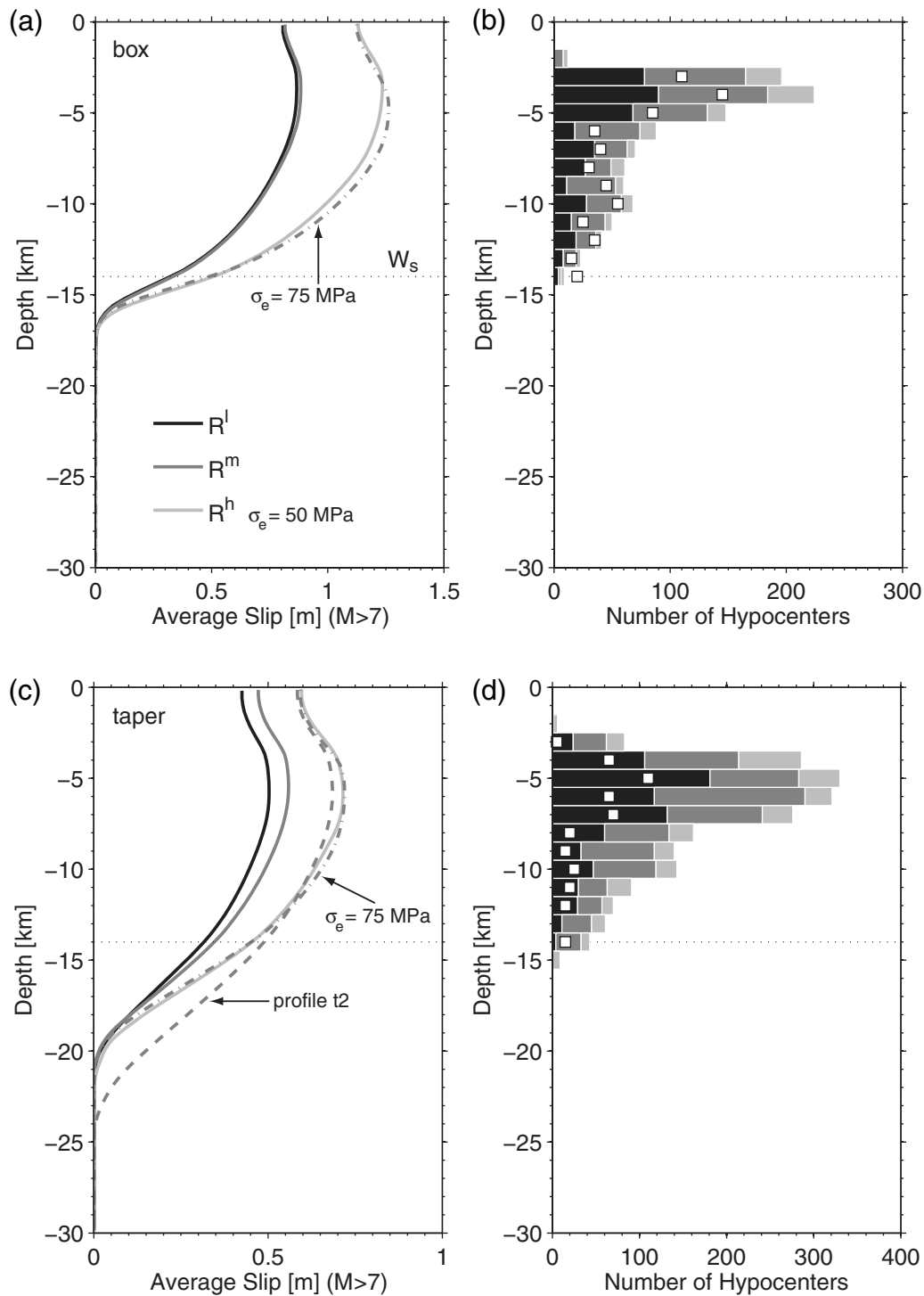


Figure 13. Average slip-depth profiles along strike for $M_L > 7$ earthquakes from (a) box and (c) taper models. Solid lines: $\sigma_e = 50$ MPa, $v^{\text{trs}} = 10^4 v^\infty$, taper models used a - b profile $t1$. Dash-dotted lines: $\sigma_e = 75$ MPa, R^m . Dashed line: a - b profile $t2$, R^m . Relative moment release above/below W_s for the box models: R^l 96%/4%, R^m 97%/3%, R^h 96%/4%, $\sigma_e = 75$ MPa 97%/3%. Taper models: R^l 86%/14%, R^m 88%/12%, R^h 87%/13%, $\sigma_e = 75$ MPa 88%/12%, $t2$ 80%/20%. (b) and (d) Hypocenter (seismicity) distribution with depth (all event sizes). White squares show number of corresponding hypocenters for $M_L > 7$ events, multiplied by five for clarity. Note different scales on the respective horizontal axes. The peak in the number of hypocenters for the taper models is lowered because of the strengthening effect of the tapered a - b profile at shallow depth.

The inferred hypocenter-depth distributions support usage of the term seismogenic zone in the present context (Fig. 13b, d). Events nucleate exclusively in regions of negative $a-b$ above 15-km depth. However, the generated distribution, with the peak of large event initiation around $z = -5$ km is at odds with the observations that large events nucleate lower and near the brittle-ductile transition (Scholz, 1988). This inconsistency can be explained with characteristics of the model, related to the manner in which the fault model is loaded (Tse and Rice, 1986). The similar shape of the corresponding slip- and hypocenter-depth distributions shows the negligible effect of the topmost velocity-strengthening part in the tapered $a-b$ profile; however, the peak in the taper case is about 2 km deeper.

Conclusion

Heterogeneous fault properties along strike and depth, and the resulting complex rupture propagation, heterogeneous slip distributions, and spatially variable stress drops of large events, remind us that the results presented in this study are a first-order approximation to properties of real seismicity. Nevertheless, based on an increasing body of evidence suggesting the occurrence of coseismic slip on localized structure below the seismogenic zone defined by background seismicity, we used a rate-and-state 3D strike-slip fault framework with a modified slip-rate-dependent profile at depth to explore the effect of rupture width on earthquake scaling relations. This procedure captures complex feedback mechanisms within the broad semibrittle midcrust region and produces synthetic data that are compatible with observations, including spatially complex slip and stress-drop distributions.

We performed systematic numerical experiments to investigate the effect of the $a-b$ gradient, trigger threshold, effective normal stress, and spatiotemporal resolution. The results show that earthquake populations confined to $W_s = 15$ km produce slip-length relations compatible with observations but show a linear dependence of stress drop on earthquake size, which is not supported by observation. In contrast, synthetic seismicity generated by a fault model with a less restrictive slip-rate dependence below W_s has larger rupture widths, consistently smaller average slip values, and consequently constant stress-drop scaling.

Event sizes and thus scaling relations have been demonstrated to be sensitive to the particular definition of coseismic-slip rates, as a result of the quasidynamic character of the numerical experiments. The numerical experiments presented here, by Das (1982) and more recently by Shaw and Wesnousky (2008), demonstrate that seismic-slip rates and scaling laws are sensitive to the boundary conditions assumed at the base of the seismogenic layer. The buried fault model of Das (1982) assumed deformation above and below the seismogenic layer to be ductile and slip to occur in the absence of stress drop or seismic radiation. The results presented here and by Shaw and Wesnousky (2008) are effec-

tively governed by friction laws for which coseismic slip below the seismogenic layer does produce stress drop and seismic radiation. Regardless of the variations in the approaches to modeling the problem, the results show that the occurrence of coseismic slip below the seismogenic layer is a physically plausible explanation of slip versus length scaling laws.

King and Wesnousky (2007) discussed the ability of coseismic slip to propagate below W_s in the context of fault-zone maturity and geometric heterogeneity. Hillers *et al.* (2007) parameterized faults at different evolutionary stages using 2D D_c distributions with different degrees and types of heterogeneity. It is thus reasonable to investigate the coevolution of fault-zone complexity (Wesnousky, 1988) and properties at depth controlling deep slip simultaneously.

The decreased growth rates and slip velocities below W_s of synthetic earthquakes with deep slip are compatible with observations that substantial portions of slow slip might not be detected in the frequency band that is sensitive to rapid slip in the seismogenic part, but at significantly longer periods (e.g., Stein and Okal, 2005). Together with the current depth resolution of geodetic and seismological observations, the results presented here might encourage more rigorous search for deep coseismic slip in nature. In the event that the model results are shown to be a good approximation of fault behavior, the characterization of earthquake dynamics and associated scaling properties should leave behind the discussion of fault-rupture processes in terms of L or W scaling behavior.

Acknowledgments

G. H. was supported by the Swiss National Science Foundation, Contribution Number PBEZ2-111586, by the James S. McDonnell Foundation, the David and Lucile Packard Foundation, and the National Science Foundation (NSF) under Grant Number DMR-0606092. S. G. W. acknowledges partial support from U.S. Geological Society (USGS) Award Number 07HQGR0108. G. H. thanks R. Archuleta for pointing toward the role of effective normal stress; M. Page, S. Custódio, and C. Ji for discussing the detectability of deep slip with geodetic and seismological techniques, respectively; L. Manning and J. Carlson for discussions on localization mechanisms; T. Little and B. Hacker for explaining sheared materials; K. Regenauer-Lieb for providing preprints; and Y. Ben-Zion for seeding the idea of dynamic strength feedbacks at depth in earlier discussions. The computational work of this study was performed on the Dragon cluster of the Institute for Crustal Studies (ICS), University of California at Santa Barbara. This is ICS Contribution Number 0816 and Center for Neotectonic Studies (CNS) Contribution Number 53.

References

- Abercrombie, R. E. (1995). Earthquake source scaling relationships from -1 to $5 M_L$ using seismograms recorded at 2.5 km depth, *J. Geophys. Res.* **100**, no. B12, 24,015–24,036.
- Ben-Zion, Y. (1996). Stress, slip, and earthquakes in models of complex single-fault systems incorporating brittle and creep deformations, *J. Geophys. Res.* **101**, no. B3, 5677–5706.
- Ben-Zion, Y. (2003). Appendix 2, key formulas in earthquake seismology, in *International Handbook of Earthquake and Engineering Seismology, Part B*, W. H. Lee, H. Kanamori, P. C. Jennings and C. Kisslinger (Editors), Academic Press, Amsterdam, 1857–1875.

- Ben-Zion, Y., and V. Lyakhovsky (2006). Analysis of aftershocks in a lithospheric model with seismogenic zone governed by damage rheology, *Geophys. J. Int.* **165**, 197–210, doi 10.1111/j.1365-246X.2006.02878.x.
- Ben-Zion, Y., and L. Zhu (2002). Potency-magnitude scaling relations for southern California earthquakes with $1.0 < M_L < 7.0$, *Geophys. J. Int.* **148**, F1–F5.
- Beresnev, I. A. (2003). Uncertainties in finite-fault slip inversions: to what extend to believe? (a critical review), *Bull. Seismol. Soc. Am.* **93**, no. 6, 2445–2458.
- Blanpied, M. L., D. A. Lockner, and J. D. Byerlee (1991). Fault stability inferred from granite sliding experiments at hydrothermal conditions, *Geophys. Res. Lett.* **18**, no. 4, 609–612.
- Bodin, P., and J. N. Brune (1996). On the scaling of slip with rupture length for shallow strike-slip earthquakes: quasi-static models and dynamic rupture propagation, *Bull. Seismol. Soc. Am.* **86**, no. 5, 1292–1299.
- Chester, F. M. (1995). A rheologic model for wet crust applied to strike-slip faults, *J. Geophys. Res.* **100**, no. B7, 13,033–13,044.
- Chester, F. M., and J. S. Chester (1998). Ultracataclastite structure and friction processes of the Punchbowl fault, San Andreas system, California, *Tectonophysics* **295**, 199–221.
- Cole, J., B. Hacker, L. Ratschbacher, J. Dolan, G. Seward, E. Frost, and W. Frank (2007). Localized ductile shear below the seismogenic zone: structural analysis of an exhumed strike-slip fault, Austrian Alps, *J. Geophys. Res.* **112**, B12304, doi 10.1029/2007JB004975.
- Das, S. (1982). Appropriate boundary conditions for modeling very long earthquakes and physical consequences, *Bull. Seismol. Soc. Am.* **72**, no. 6, 1911–1926.
- Hanks, T. C. (1977). Earthquake stress drops, ambient tectonic stresses and stresses that drive plate motions, *Pure Appl. Geophys.* **115**, 441–458.
- Heimpel, M. H. (2003). Characteristic scales of earthquake rupture from numerical models, *Nonlinear Process. Geophys.* **10**, 573–584.
- Hillers, G. (2006). On the origin of earthquake complexity in continuum fault models with rate and state friction, *Ph.D. Thesis*, Swiss Federal Institute of Technology, Zurich (available at <http://hdl.handle.net/2122/1024>; last accessed April 2008).
- Hillers, G., and S. A. Miller (2006). Stability regimes of a dilatant, fluid infiltrated fault plane in a 3-d elastic solid, *J. Geophys. Res.* **111**, B08304, doi 10.1029/2005JB003872.
- Hillers, G., and S. A. Miller (2007). Dilatancy controlled spatiotemporal slip evolution of a sealed fault with spatial variations of the pore pressure, *Geophys. J. Int.* **168**, 431–445, doi 10.1111/j.1365-246X.2006.03167.x.
- Hillers, G., Y. Ben-Zion, and P. M. Mai (2006). Seismicity on a fault with rate- and state dependent friction and spatial variations of the critical slip distance, *J. Geophys. Res.* **111**, B01403, doi 10.1029/2005JB003859.
- Hillers, G., P. M. Mai, Y. Ben-Zion, and J. P. Ampuero (2007). Statistical properties of seismicity of fault zones at different evolutionary stages, *Geophys. J. Int.* **169**, 515–533, doi 10.1111/j.1365-246X.2006.03275.x.
- Kagan, Y. Y. (2002). Aftershock zone scaling, *Bull. Seismol. Soc. Am.* **92**, no. 2, 641–655.
- Kanamori, H. (1977). The energy release in great earthquakes, *J. Geophys. Res.* **82**, 2981–2987.
- Kanamori, H., and D. L. Anderson (1975). Theoretical basis of some empirical relations in seismology, *Bull. Seismol. Soc. Am.* **65**, 1073–1096.
- King, G. C. P., and S. G. Wesnously (2007). Scaling of fault parameters for continental strike-slip earthquakes, *Bull. Seismol. Soc. Am.* **97**, no. 6, 1833–1840, doi 10.1785/0120070048.
- Lachenbruch, A. H., and J. H. Sass (1980). Heat flow and energetics of the San Andreas fault zone, *J. Geophys. Res.* **85**, 6185–6222.
- Lapusta, N., J. R. Rice, Y. Ben-Zion, and G. Zheng (2000). Elastodynamic analysis for slow tectonic loading with spontaneous rupture episodes on faults with rate- and state-dependent friction, *J. Geophys. Res.* **105**, no. B10, 23,765–23,789.
- Liu-Zeng, J., T. Heaton, and C. DiCaprio (2005). The effect of slip variability on earthquake slip-length scaling, *Geophys. J. Int.* **162**, 841–849, doi 10.1111/j.1365-246X.2005.02679.x.
- Mai, P. M., and G. Beroza (2000). Source scaling properties from finite-fault-rupture models, *Bull. Seismol. Soc. Am.* **90**, no. 3, 604–615.
- Mai, P. M., and G. Beroza (2002). A spatial random field model to characterize complexity in earthquake slip, *J. Geophys. Res.* **107**, no. B11, 2308, doi 10.1029/2001JB000588.
- Manighetti, I., M. Campillo, S. Bouley, and F. Cotton (2007). Earthquake scaling, fault segmentation, and structural maturity, *Earth Planet. Sci. Lett.* **253**, 429–438, doi 10.1016/j.epsl.2006.11.004.
- Marone, C., and C. H. Scholz (1988). The depth of seismic faulting and the upper transition from stable to unstable slip regimes, *Geophys. Res. Lett.* **15**, 621–624.
- Marone, C. J., C. H. Scholz, and R. Bilham (1991). On the mechanics of earthquake afterslip, *J. Geophys. Res.* **96**, no. B5, 8441–8452.
- Matsuura, M., and T. Sato (1997). Loading mechanisms and scaling relations of large interplate earthquakes, *Tectonophysics* **277**, 189–198.
- Miller, S. A. (2002). Earthquake scaling and the strength of seismogenic faults, *Geophys. Res. Lett.* **29**, no. 10, 1389, doi 10.1029/2001GL014181.
- Molnar, P., H. J. Anderson, E. Audoin, D. Eberhart-Phillips, K. R. Gledhill, E. R. Klosko, T. V. McEvilly, D. Okaya, M. K. Savage, T. Stern, and F. T. Wu (1999). Continuous deformation versus faulting through the continental lithosphere of New Zealand, *Science* **286**, 516–519, doi 10.1126/science.286.5439.516.
- Norris, R. J., and A. F. Cooper (2003). Very high strains recorded in mylonites along the Alpine fault, New Zealand: implication for the deep structure of plate boundary faults, *J. Struct. Geol.* **25**, 2141–2158.
- Passchier, C. W. and R. A. J. Trouw (Editors) (2005). *Microtectonics*, Second Ed., Springer, Berlin.
- Peng, Z., J. E. Vidale, C. Marone, and A. Rubin (2005). Systematic variations in recurrence interval and moment of repeating aftershocks, *Geophys. Res. Lett.* **32**, L15301, doi 10.1029/2005GL022626.
- Regenauer-Lieb, K., and D. A. Yuen (2007). Multiscale brittle-ductile coupling and genesis of slow earthquakes, *Pure Appl. Geophys.* (in press).
- Regenauer-Lieb, K., R. F. Weinberg, and G. Rosenbaum (2006). The effect of energy feedbacks on continental strength, *Nature* **442**, no. 6, 67–70, doi 10.1038/nature04868.
- Rice, J. R. (1992). Fault stress states, pore pressure distributions, and the weakness of the San Andreas fault, in *Fault Mechanics and Transport Properties in Rocks*, B. Evans and T.-F. Wong (Editors), Academic Press, San Diego, California, 475–503.
- Rice, J. R. (1993). Spatio-temporal complexity of slip on a fault, *J. Geophys. Res.* **98**, no. B6, 9885–9907.
- Ripperger, J., J.-P. Ampuero, P. M. Mai, and D. Giardini (2007). Earthquake source characteristics from dynamic rupture with constrained stochastic fault stress, *J. Geophys. Res.* **112**, B04311, doi 10.1029/2006JB004515.
- Rolandone, F., R. Bürgmann, and R. M. Nadeau (2004). The evolution of the seismic-aseismic transition during the earthquake cycle: constraints from the time-dependent depth distribution of aftershocks, *Geophys. Res. Lett.* **31**, L23610, doi 10.1029/2004GL021379.
- Romanowicz, B. (1992). Strike-slip earthquakes on quasi-vertical transcurrent faults: inferences for general scaling relations, *Geophys. Res. Lett.* **19**, no. 5, 481–484.
- Schaff, D. P., G. H. R. Bokelmann, G. C. Beroza, F. Waldhauser, and W. L. Ellsworth (2002). High-resolution image of the Calaveras fault seismicity, *J. Geophys. Res.* **107**, no. B9, 2186, doi 10.1029/2001JB000633.
- Scholz, C. H. (1982). Scaling laws for large earthquakes: consequences for physical models, *Bull. Seismol. Soc. Am.* **72**, no. 1, 1–14.
- Scholz, C. H. (1988). The brittle-plastic transition and the depth of seismic faulting, *Geol. Rundt.* **77**, 319–328.
- Scholz, C. H. (1994). A reappraisal of large earthquake scaling, *Bull. Seismol. Soc. Am.* **84**, no. 1, 215–218.

- Scholz, C. H. (1997). Size distributions for large and small earthquakes, *Bull. Seismol. Soc. Am.* **87**, no. 4, 1074–1077.
- Shaw, B. E. (2004). Dynamic heterogeneities versus fixed heterogeneities in earthquake models, *Geophys. J. Int.* **156**, 275–286, doi 10.1111/j.1365-246X.2003.02134.x.
- Shaw, B. E., and C. Scholz (2001). Slip-length scaling in large earthquakes: observations and theory and implications for earthquake physics, *Geophys. Res. Lett.* **28**, no. 15, 2991–2994.
- Shaw, B. E., and S. G. Wesnousky (2008). Slip-length scaling in large earthquakes: the role of deep penetrating slip below the seismogenic layer, *Bull. Seismol. Soc. Am.* **98** (in press).
- Shibazaki, B. (2005). Nucleation process with dilatant hardening on a fluid-infiltrated strike-slip fault model using a rate- and state-dependent friction law, *J. Geophys. Res.*, **110**, B11308, doi 10.1029/2005JB003741.
- Shibazaki, B., H. Tanaka, H. Horikawa, and Y. Iio (2002). Modeling slip processes at the deeper part of the seismogenic zone using a constitutive law combining friction and flow laws, *Earth Planet. Space* **54**, 1211–1218.
- Sibson, R. H. (1980). Transient discontinuities in ductile shear zones, *J. Struct. Geol.* **2**, no. 1/2, 165–171.
- Stein, S., and E. A. Okal (2005). Speed and size of the Sumatra earthquake, *Science* **434**, 581–582.
- Stesky, R. M. (1975). The mechanical behavior of faulted rock at high temperature and pressure, *Ph.D. thesis*, Massachusetts Institute of Technology, Cambridge, Massachusetts.
- Tse, S. T., and J. R. Rice (1986). Crustal earthquake instability in relation to the depth variation of frictional slip properties, *J. Geophys. Res.* **91**, no. B9, 9452–9472.
- Wells, D. L., and K. J. Coppersmith (1994). New empirical relationships among magnitude, rupture length, rupture width, rupture area, and surface displacement, *Bull. Seismol. Soc. Am.* **84**, no. 4, 974–1002.
- Wesnousky, S. G. (1988). Seismological and structural evolution of strike-slip faults, *Nature* **335**, 340–343.
- Wesnousky, S. G. (2008). Displacement and geometrical characteristics of earthquake surface ruptures: issues and implications for seismic-hazard analysis and the process of earthquake rupture, *Bull. Seismol. Soc. Am.* **98** (in press).
- Wilson, C. K., C. H. Jones, P. Molnar, A. F. Sheehan, and O. S. Boyd (2004). Distributed deformation in the lower crust and upper mantle beneath a continental strike-slip fault zone: Marlborough fault system, South Island, New Zealand, *Geology* **32**, no. 10, 837–840, doi 10.1130/G20657.1.
- Yin, Z.-M., and G. Rogers (1996). Toward a physical understanding of earthquake scaling relations, *Pure Appl. Geophys.* **146**, 661–675.
- Zöller, G., M. Hohlschneider, and Y. Ben-Zion (2005). The role of heterogeneities as a tuning parameter of earthquake dynamics, *Pure Appl. Geophys.* **162**, 1027–1049, doi 10.1007/s00024-004-2660-9.

Institute for Crustal Studies
Girvetz Hall 1140
University of California
Santa Barbara, California, 93106-1100
gregor@crustal.ucsb.edu
(G.H.)

Center for Neotectonic Studies
Mail Stop 169
University of Nevada
Reno, Nevada 89557
stevew@seismo.unr.edu
(S.G.W.)

Manuscript received 7 August 2007